turbulence structure and scalar transfer mechanisms. A numerical technique is a promising tool to complement measurements of processes that cannot be clarified by turbulence measurements in environmental flows. It should also be noted that most of the interesting phenomena in environmental flows can be elucidated by laboratory or field measurements but not by numerical simulations alone. Thus, it is of importance to combine laboratory or field measurements with numerical simulations in clarifying environmental flow phenomena.

This report summarizes research on two turbulence structure and diffusion topics; turbulence structure and the gas transfer mechanism across the air-sea (air-water) interface and the heat and momentum transfer mechanism in thermally stratified flows. The first study shows the relationship between the carbon dioxide (CO_2) transfer mechanism across a sheared air-water interface and the turbulence structure near the interface. The results revealed that the conventional proportional relationship between CO_2 transfer velocity across the air-sea interface and mean wind speed over the sea surface is incorrect. The second study numerically clarified the significant effects of molecular diffusivity (the Prandtl number) of active heat on heat transfer in stable thermally-stratified flows. The results obtained from the two studies are described in the next two chapters. Since the results are mainly quoted from a series of previously published and in press works by Komori et al.'s research group (see references), this report might be considered as a summary of those works.

2. TURBULENCE STRUCTURE AND THE MECHANISM OF CO_2 TRANSFER AT THE AIR-SEA INTERFACE

2.1 What Are the Problems in Estimating the Rate of CO_2 Transfer Across the Air-Sea Interface ?

The amount of carbon dioxide released from fossil fuel combustion is increasing year by year and numerical simulations by general circulation models (GCMs) warn that the rising atmospheric CO_2 concentration will cause significant global climate change in the near future. However the predictions are rather uncertain, since the global atmospheric CO_2 budget has not been precisely estimated. In particular the CO_2 exchange mechanism between the atmosphere and the ocean has not been well investigated, and therefore a method for precise estimation of the rate of CO_2 exchange across the air-sea interface is strongly desired. On the other hand, biological fixation of CO_2 in the ocean surface layer is being planned to reduce industrial CO_2 released into the atmosphere. To design such an effective CO_2 fixation process, it is also of practical importance to estimate precisely the CO_2 transfer rate across the air-sea interface.

The CO_2 transfer velocity across the air-sea interface has been measured by a number of investigators in the field (Jahne 1980; Roether and Kromer 1984; Brocker et al. 1986; Roether 1986; Watson et al. 1991). However, there is a lot of scatter in these field data

among the various studies. The scattered data resulted in the rough correlation that shows a linear proportionality between transfer velocity and wind speed. Although the proportionality was also supported by a number of laboratory measurements (Liss and Merlivat 1986 and others), no reasonable physical explanation of why transfer velocity should be directly proportional to wind speed has been published. Most previous field and laboratory studies on mass transfer have tried only to find such a proportional relationship between transfer velocity and wind speed or friction velocity, and have not succeeded in explaining the physical gas transfer mechanism across a wavy air-water interface.

It is, therefore, of great importance to both numerically and experimentally investigate the relationship between CO_2 transfer velocity across a wavy sheared air-water interface and wind speed or friction velocity to precisely estimate the velocity of CO_2 transfer across the air-sea interface. Komori et al.(1995a) measured the CO_2 transfer velocity for fresh water in a wind-wave tunnel by carrying out CO_2 desorption experiments. They also investigated turbulence structure by means of both direct numerical simulations (DNSs) and instantaneous velocity measurements in air and water flows above and below the air-water interface. In addition, Komori and Shimada (1995) carried out CO_2 absorption experiments in an oscillating-grid tank to investigate the effects of natural sea water on the CO_2 transfer velocity. From the laboratory measurements of CO_2 transfer velocities in both fresh and sea waters, Komori and Shimada (1995) proposed a method to estimate the CO_2 transfer velocity across the air-sea interface.

2.2 Direct Numerical Simulations for Investigating Turbulence Structure and the Mechanism of CO_2 Transfer Across an Air-Water Interface

2.2.1 Why is DNS useful ?

Direct numerical simulations (DNSs) of time-dependent three-dimensional Navier-Stokes (NS) equations have often been used in the fields of engineering and physics. The DNS for low Reynolds numbers (Re < 10,000) is replacing sophisticated experimental techniques such as an image-processing technique, because DNS can directly predict instantaneous velocity and pressure in the computational domain. These capabilities suggest that DNS can not only overcome the disadvantages of experiments, but that it can also become a powerful tool to resolve the details of flow structure in the region near wavy sheared air-water interfaces. Although it is very difficult to measure instantaneous velocity and pressure near a moving, wavy air-water interface, DNS can provide turbulence quantities such as the velocity-pressure correlation in the interfacial region. In addition, DNS has the great advantage that it can be easily used to investigate the mechanism of mass transfer across an air-water interface by solving the mass diffusion equations with NS equations. Although the turbulence structure near an air-water interface has been mainly inferred from flow visualization, Lam and Banerjee (1988; 1992) first applied DNS to an open-channel flow and tried to explain the measurements of Komori et al.(1982). However, they treated the free

surface as a rigid slip wall in their DNS based on the pseudospectral method. Until the initial work by Komori et al. (1993b), there had been no DNS study treating an air-water interface realistically.

2.2.2 Numerical procedure for DNS

A coordinate system which can describe a free surface is shown in Fig.1 (Komori et al. 1993b). Subscripts 1, 2 and 3 denote the streamwise, spanwise, and vertical directions, respectively. The equations governing the flow in an incompressible Newtonian fluid are:

$$\frac{\partial v_i}{\partial x_i} = 0 , \tag{1}$$

$$\frac{\partial v_i}{\partial t} + v_j \frac{\partial v_i}{\partial x_j} = -\frac{1}{\rho}\frac{\partial p}{\partial x_i} + \nu \frac{\partial^2 v_i}{\partial x_j \partial x_j} + g\delta_{i3} , \tag{2}$$

where v_i is the i-th component of the velocity vector, p is the pressure, ν is the kinematic viscosity, g is the acceleration of gravity, ρ is the density, and δ_{ij} denotes Kroneker's delta.

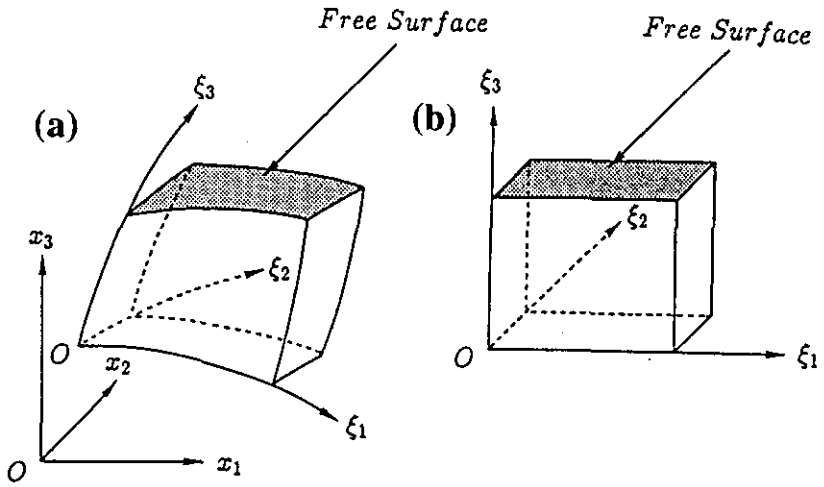

Figure 1. The coordinate system: (a) physical region; (b) computational region (Komori et al. 1993b).

When mass transfer occurs, the instantaneous concentration of a non-reacting passive mass, c, is given by

$$\frac{\partial c}{\partial t} + v_j \frac{\partial c}{\partial x_j} = D \frac{\partial^2 c}{\partial x_j \partial x_j} , \tag{3}$$

where D is the molecular diffusivity of the mass. The Einstein summation convention is also used. In both streamwise and spanwise directions, the periodic boundary condition was used for all velocities and pressure. On the free surface, two boundary conditions should be

satisfied. One is the kinematic boundary condition that describes the Lagrangian behavior of the fluid particle on the free surface, and the other is the dynamical boundary condition which is determined from the balance of stresses acting on the interface in the normal and tangential directions:

$$\frac{\partial F}{\partial t} + v_i \frac{\partial F}{\partial x_i} = 0 , \tag{4}$$

$$p + \sigma_n + p_s = p_0 , \tag{5}$$

$$\sigma_n = \mu e_{ij} n_j n_i , \tag{6}$$

$$p_s = \gamma \kappa_m , \tag{7}$$

$$\sigma_t = \mu e_{ij} n_j t_i = 0 , \tag{8}$$

where F, σ_n, p_s, p_0, μ, e_{ij}, v_i, γ, κ_m, σ_t and t_i are, respectively, the functions expressing the form of the free surface, the normal component of the viscous force vector, the pressure variation due to surface tension, the pressure on the gas side, the viscosity, the deformation rate tensor, the unit vector in the normal direction, the surface tension, the mean curvature of the free surface, the tangential component of the viscous force vector and the unit vector in the tangential direction. The boundary conditions at an air-water interface are also shown in Fig.2. The boundary condition for the mass concentration is given by

$$c = c^* , \tag{9}$$

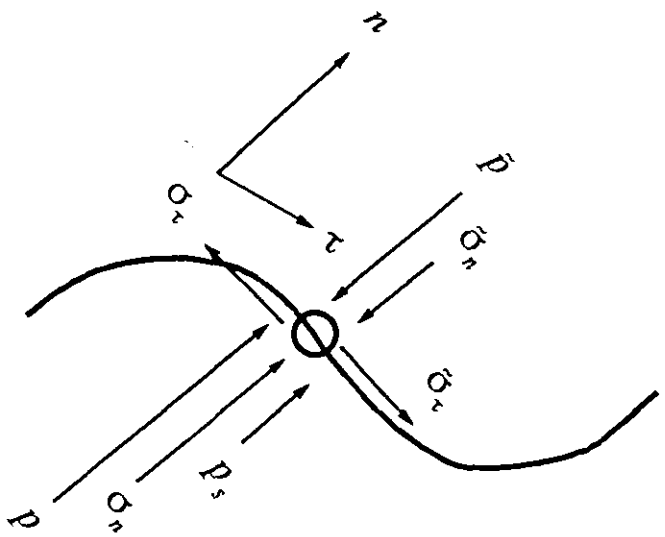

Figure 2. Boundary conditions at an air-water interface.

where c^* is the equilibrium concentration at the interface, c *.

Introducing the characteristic velocity and length, V and L, we obtain a set of the reference values:

$$v^* = v/V,\quad x^* = x/L,\quad p^* = p/\rho V^2,\quad Re = VL/\nu,\quad Fr = V^2/gL,\quad \gamma^* = \gamma/\rho LV^2,$$
$$e_{ij}^* = e_{ij}Re/\rho V^2,\quad \kappa_m^* = \kappa_m L,\quad F^* = F/L,\quad t^* = tV/L\,. \tag{10}$$

Normalizing Eqs.(1) ~ (9) by the characteristic velocity and length and the bulk concentration in the air flow, we obtain a set of nondimensional governing equations and boundary conditions:

$$\frac{\partial v_i}{\partial x_i} = 0\,, \tag{11}$$

$$\frac{\partial v_i}{\partial t} + v_j\frac{\partial v_i}{\partial x_j} = -\frac{\partial P}{\partial x_i} + \frac{1}{\mathrm{Re}}\frac{\partial^2 v_i}{\partial x_j \partial x_j}\,, \tag{12}$$

$$P = p - \frac{1}{Fr}(x_3 - x_{30}) \tag{13}$$

$$\frac{\partial c}{\partial t} + v_j\frac{\partial c}{\partial x_j} = Sc\,\mathrm{Re}\frac{\partial^2 c}{\partial x_j \partial x_j}\,, \tag{14}$$

$$\frac{\partial F}{\partial t} + v_i\frac{\partial F}{\partial x_i} = 0\,, \tag{15}$$

$$p + \frac{1}{\mathrm{Re}}e_{ij}n_j n_i + \gamma\kappa_m = p_0\,, \tag{16}$$

$$\sigma_t = e_{ij}n_j t_i = 0\,, \tag{17}$$

$$c = c^*\,, \tag{18}$$

where the pressure, P , is the reference pressure involving the effect of gravity and x_{30} denotes the height of the reference position, which corresponds to the averaged interface.

The marker and cell (MAC) method was used to solve the governing equations. The pressure Poisson equation (hereafter referred to as the P-P equation) was derived from the divergence of the NS equations:

$$\frac{\partial^2 P}{\partial x_i \partial x_i} = -\frac{\partial}{\partial x_i}(v_j \frac{\partial v_i}{\partial x_j}) + \frac{1}{\mathrm{Re}} \frac{\partial^2 D}{\partial x_i \partial x_i} - \frac{\partial D}{\partial t}, \tag{19}$$

where $D = \partial v_i / \partial x_i$. Integrating Eq.(19) from $t = n\Delta t$ to $(n+1)\Delta t$, we obtain

$$\frac{\partial^2 P}{\partial x_i \partial x_i}\Delta t = -\frac{\partial}{\partial x_i}(v_j \frac{\partial v_i}{\partial x_j})\Delta t + (\frac{1}{\mathrm{Re}} \frac{\partial^2 D^n}{\partial x_i \partial x_i}\Delta t - (D^{n+1} - D^n)), \tag{20}$$

where Δt is the time increment. Substituting the equation of continuity ($D^{n+1} = 0$) into Eq.(13), we finally obtain,

$$\frac{\partial^2 P}{\partial x_i \partial x_i} = -\frac{\partial}{\partial x_i}(v_j \frac{\partial v_i}{\partial x_j}) + (\frac{1}{\mathrm{Re}} \frac{\partial^2 D}{\partial x_i \partial x_i} + \frac{D}{\Delta t}), \tag{21}$$

The velocity vector, v_i , and the pressure can be determined by alternately solving the NS equation of Eqs.(12) and (13) and the P-P equation of Eq.(21). This numerical procedure is the outline of the MAC method used.

The boundary conditions for the NS equation at the zero-shear free surface are the divergence-free condition on the liquid side and the balance of the tangential stress in the streamwise directions. The boundary condition for the P-P equation at the free surface is given by taking the balance of the normal stress described by Eq.(16). When the deformation of the free surface is limited to non-breaking waves, the kinematic boundary condition of Eq.(15) at the free surface can be rewritten using a single-valued function f of x_1 and x_2:

$$\frac{\partial f}{\partial t} + v_1 \frac{\partial f}{\partial x_1} + v_2 \frac{\partial f}{\partial x_2} = v_3, \tag{22}$$

where f is defined by

$$F(x_1, x_2, x_3, t) = f(x_1, x_2, t) - x_3 = 0. \tag{23}$$

The NS equation, the P-P equation and kinematic boundary conditions were transformed into the generalized equations based on the boundary-fit coordinate system (Komori et al. 1993b).

The transformed governing equations were discretized to construct the finite-difference formulation. The nonlinear terms appearing in the NS equation and the kinematic boundary conditions were approximated by a fifth-order upwind scheme:

$$(v\frac{\partial v}{\partial \xi})_i = v_i \frac{v_{i+3} - 9v_{i+2} + 45(v_{i+1} - v_{i-1}) + 9v_{i-2} - v_{i-3}}{60\Delta\xi} + |v_i| \frac{v_{i+3} - 6v_{i+2} + 15v_{i+1} - 20v_i + 15v_{i-1} - 6v_{i-2} + v_{i-3}}{60\Delta\xi} \tag{24}$$

Other spatial derivatives were approximated by a second-order central difference, i.e.,

$$(\frac{\partial v}{\partial \xi})_i = \frac{v_{i+1} - 2v_i + v_{i-1}}{\Delta\xi^2} . \tag{25}$$

The finite-difference equations were finally obtained by discretizing the transformed equations by Eqs.(24) and (25). The time integration of the NS equation was carried out by a second-order Runge-Kutta method and the Crank-Nicolson method was used for the kinematic boundary conditions. The mass diffusion equation was simultaneously solved with the governing equations. The discretization and time integration for the mass diffusion equation were similar to those used with the NS equation.

The computational domain for a sheared wavy air-water interface (Fig.3) was 50, 20 and

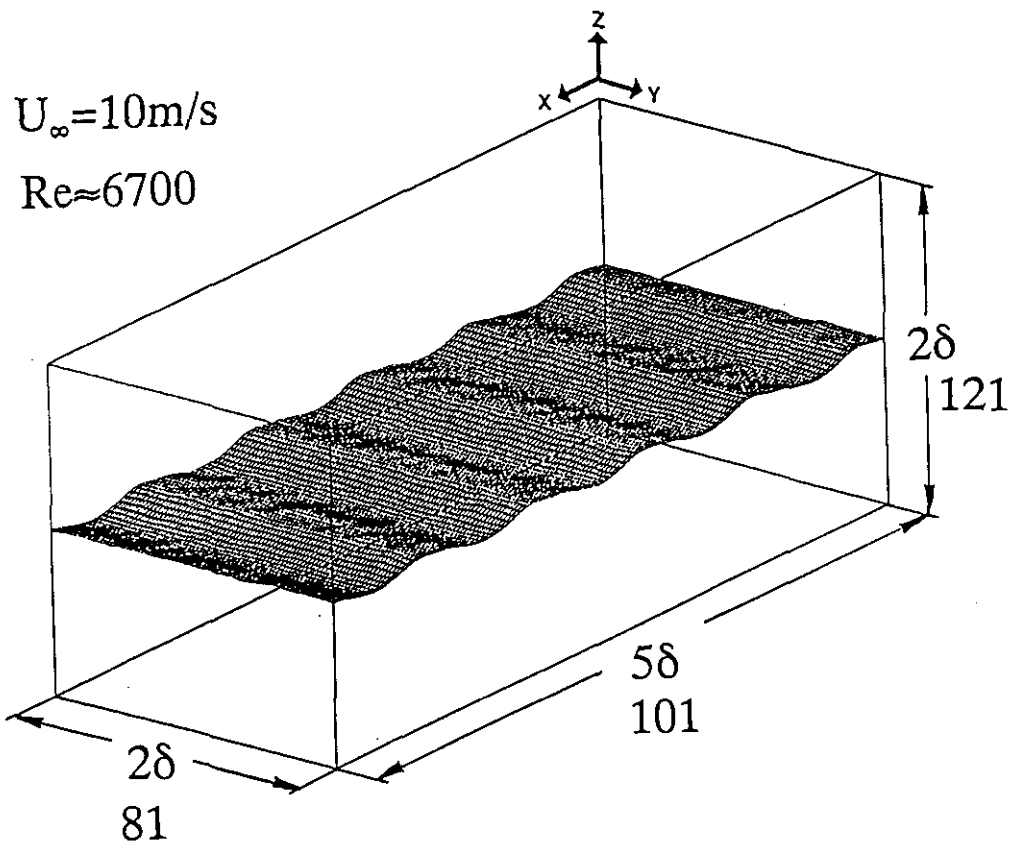

Figure 3. The geometry and grid system of computational region for a sheared wavy air-water interface.

20 times the averaged wave height in the streamwise, spanwise and vertical directions, respectively. The Reynolds number based on the maximum wave height, h, and the uniform air velocity, U, was about 6,700. The grid points used were 101 × 81 × 121 in the streamwise, spanwise and vertical directions, respectively. The accuracy of the DNS was discussed by Komori et al. (1993b).

In addition to the DNS for a sheared wavy air-water interface, two DNS's were conducted for air flows over two and three dimensional rigid wavy walls to investigate the difference between organized motions over two and three dimensional waves. Figures 4 and 5 show the computational domains for two and three dimensional wavy walls. The numerical procedure used with these DNS's was the same as that used in the DNS for an air-water

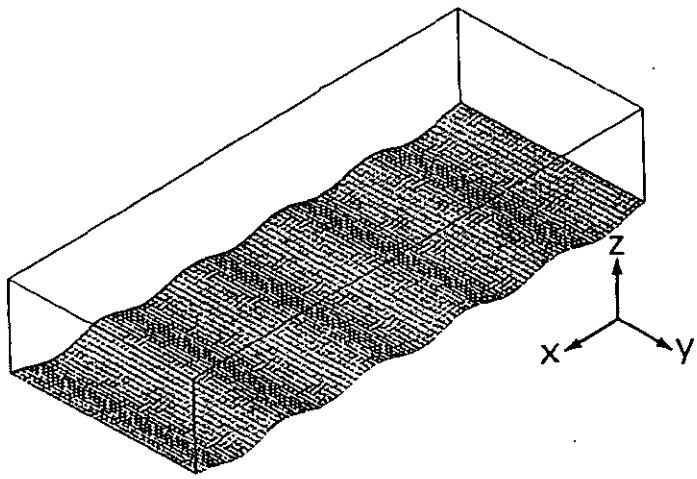

Figure 4. The geometry and grid system of the computational region for a two dimensional wavy wall.

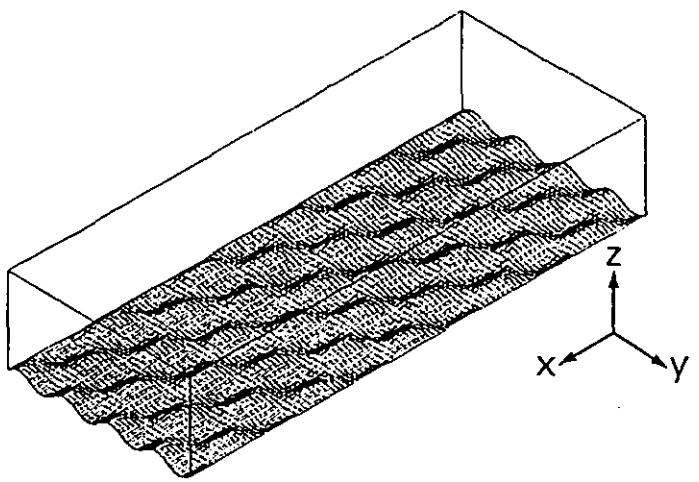

Figure 5. The geometry and grid system of the computational region for a three dimensional wavy wall.

interface. The computational domain was 50, 20 and 10 times the averaged wavy-wall height in the streamwise, spanwise and vertical directions, respectively. The Reynolds number based on the wavy-wall height and the uniform air velocity was about 6,700. The grid points used were $101 \times 81 \times 61$ in the streamwise, spanwise and vertical directions, respectively.

2.3 Laboratory Measurements of CO_2 Transfer Velocity

2.3.1 Experiments for investigating the mechanism of CO_2 transfer

The details of the wind-wave tunnel used in a series of works (Komori et al. 1993a; 1995a; Komori and Shimada 1995; Fig.6) are described in Komori et al. (1993a). Nonlinear three-dimensional waves with various conditions were driven in the wind-wave tank by winds with a free-stream velocity of 2~20 m/s. Wind waves intensively broke for a high free-stream velocity of $U > 14$ m/s, and many bubbles and spray droplets were entrained into the water and air flows, respectively.

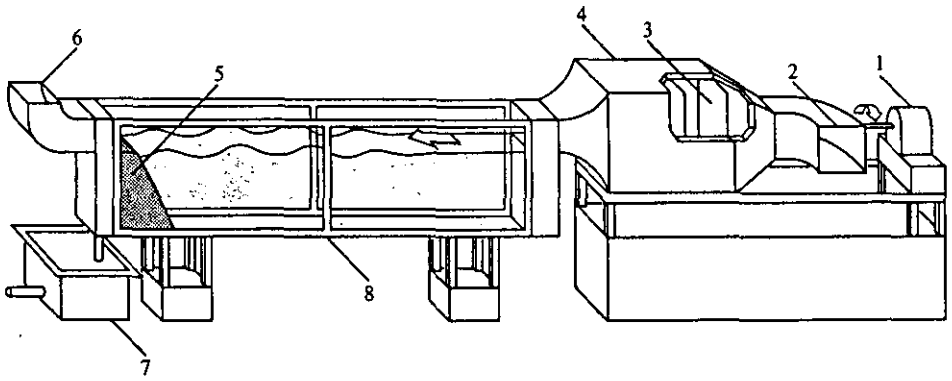

Figure 6. Schematic diagram of the wind-wave tank (Komori et al. 1993a; 1995a) :
1) motor; 2) air inlet; 3) screen; 4) wind tunnel; 5) wave absorber;
6) air outlet; 7) drain tank; 8) wind-wave tank

Instantaneous streamwise and vertical wind velocities in the air flow were simultaneously measured with a constant-temperature hot-wire anemometer with a miniature X-probe. Streamwise and vertical velocities in the water flow were measured using a two-color laser-Doppler velocimeter in forward scattering mode. The hot-wire and laser probes were vertically traversed up to just above the crests and below the valleys of the waves, respectively. To detect the surface-renewal eddies that control mass transfer, simultaneous measurements of vertical and streamwise velocities and temperature, i.e. instantaneous vertical heat flux and Reynolds stress measurements, were conducted in the same wind-wave tank with slightly heated water. Both a laser Doppler velocimeter and a miniature cold-film probe operated by a constant current temperature bridge were used for these simultaneous measurements. When surface-renewal eddies appear at the air-water interface and are cooled by the air, negative spikes occur in the time records of both instantaneous vertical heat flux

and Reynolds stress. Therefore, the frequency of appearance of the surface renewal eddies could be estimated by counting these negative spikes (Komori et al. 1993a; 1995a).

In addition to the velocity measurements, flow visualization was carried out in both the air and water flows. For the air flow, a smoke-wire technique was adopted and a paraffin mist was introduced over the waves. In the water flow, sodium fluorescein dye was introduced and it was illuminated by a high-power argon-ion laser. The flow patterns of smoke and dye were viewed from the side wall of the wind-wave tank and they were recorded at an interval of 0.0025 sec with a high-speed video system. Each frame of the recorded pictures was carefully analyzed.

The CO_2 transfer across an air-water interface is determined by transport process on the water side, since the transfer resistance on the air side is negligibly small compared to that on the water side. Therefore, the mass transfer velocity on the water side, k_L, was measured by monitoring CO_2 desorption from the water to the air. First, pure CO_2 was dissolved to excess into filtered tap water stored in the wind-wave tank and homogeneously mixed. Then the wind tunnel fan was turned on and the mean concentration of CO_2 desorbed from water to air was measured vertically at two locations in the air flow with two sampling tubes connected to infrared spectroscopic CO_2 analyzers. The bulk CO_2 concentration on the water side was measured from a sampling tube connected to a total organic carbon analyzer, and pH was measured with a pH meter. From these concentration measurements, the rate of CO_2 desorption from the water into the air was estimated by establishing the mass balance in the air flow and then the CO_2 transfer velocity on the water side was calculated by:

$$N = k_L (C_b - C^*) = k_L S \Delta p_{CO2}, \tag{26}$$

where N is the desorption rate per unit area, C_b is the bulk CO_2 concentration on the water side, C^* is the equilibrium CO_2 concentration at 20°C and 1atm, S is the solubility of CO_2 in water and Δp_{CO2} is the CO_2 partial pressure difference between the air and water.

Mean CO_2 concentration measurements in the air flow were limited to the wind speed range of U < 14 m/s, because the many spray droplets entrained by intense wave breaking prevented us from measuring the CO_2 concentration in the air flowing at higher speeds. However, despite the high mass transfer rate due to wave breaking, we were able to estimate the CO_2 transfer rate from the mass balance on the water side. That is, the time variation of mean CO_2 concentration in the water flow becomes rather large at wind speeds > 14 m/s, while streamwise (x) convection and diffusion of CO_2 in the water flow were negligibly small compared to the time derivative of CO_2 concentration in the mass diffusion equation. Thus, the desorption rate for wind speeds > 14 m/s was calculated from the time variation of the vertical (y) CO_2 concentration profile in the water flow, i.e. by taking the mass balance on the water side.

To investigate the effects of natural sea water on the CO_2 transfer velocity, CO_2 absorption experiments were carried out in a small oscillating-grid tank (Fig.7). Five water types - pure, filtered tap, natural sea, artificial sea and 3.5 wt% salt waters - were used in the tank with 0.5 m^3 volume. Pure CO_2 at 1 atm was filled over the gas-liquid interface in the closed tank and the absorption rate was measured using a soap-film meter. The CO_2 transfer velocities for the five waters were calculated from the measured absorption rates using equation (26). The frequency of appearance of surface renewal eddies in the oscillating-grid tank was estimated through measurements of the instantaneous Reynolds stress beneath the gas-liquid interface by means of a laser Doppler velocimeter.

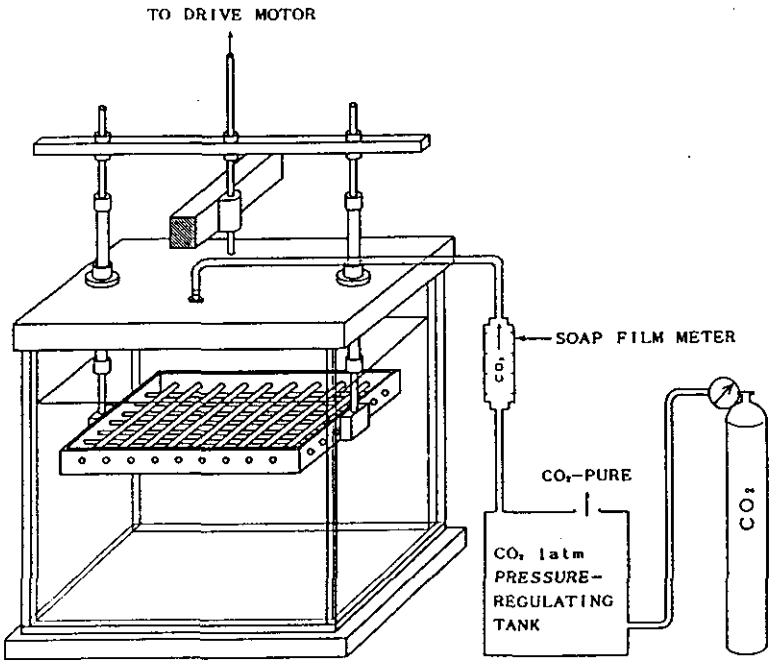

Figure 7. Schematic of the oscillating-grid tank (Komori et al. 1995a).

2.3.2 Correlation between CO_2 transfer velocity and wind speed or friction velocity

Figure 8 shows the CO_2 transfer velocity measured by Komori et al. (1995a) and Komori and Shimada (1995) against wind speed and friction velocity, u^*, together with previous laboratory measurements. The CO_2 transfer velocity, k_L, measured by Komori et al. (1995a) and Komori and Shimada (1995) rapidly increases with increasing U or u^* in the low wind speed region of 2 m/s < U < 5 m/s (0.06 m/s < u^* < 0.22 m/s), where capillary-gravity waves are present. At U = 5 m/s, k_L reaches about ten times the values measured in open-channel flows with unsheared (zero-shear) air-water interfaces ($k_L < 2\times10^{-5}$ m/s) (Komori et al. 1989; 1990). This result means that mass transfer is greatly facilitated in the presence of interfacial wind shear. However, the tendency of k_L to increase with increasing wind speed levels off in the high wind speed region of 5 m/s < U < 12 m/s (0.22 m/s < u^* < 0.83

m/s). In this wind speed range, wind waves are rapidly developing. The physical reason for this flattening of k_L - wind speed function will be explained in the next section. When wind speeds exceed 12 m/s ($u^* > 0.83$ m/s), k_L again increases rapidly with wind speed. In the high wind speed region, waves break intensively and many surface renewal (ripple-like) eddies with small scales comparable to those of the wave heights are generated. In addition, many bubbles and spray droplets are entrained into the water and air flows respectively. The wave breaking phenomena contribute to the enhancement of k_L at $U > 12$ m/s ($u^* > 0.83$ m/s).

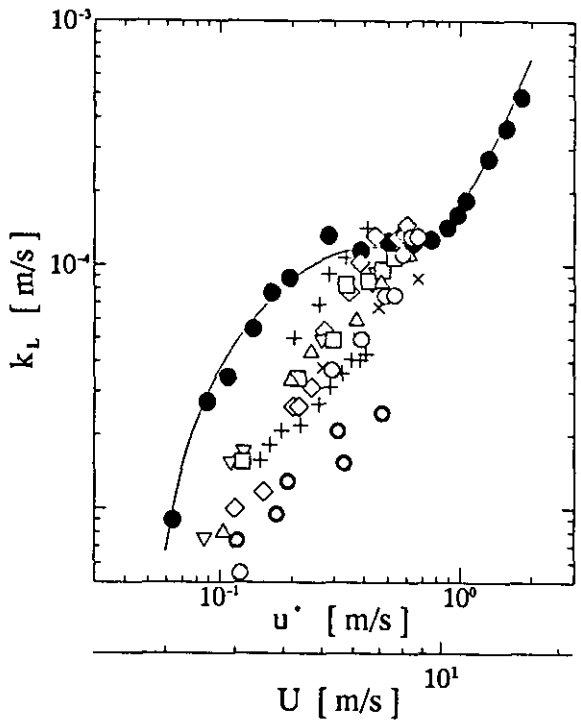

Figure 8. Variations of CO_2 transfer velocity (●) with mean wind speed, U, and wind friction velocity, u^*, and comparisons with previous laboratory measurements (other symbols) (Komori and Shimada 1995).

The relationship between k_L and wind speed described here is rather different from those derived from previous laboratory measurements (Liss 1973; Broecker et al. 1978; Merlivat and Memery 1983; Wanninkhof and Bliven 1991) that show simple proportional correlations between k_L and U. The difference in the region of 5 m/s $< U <$ 12 m/s where the present k_L levels off, is due to errors in CO_2 flux measurements in the previous studies, as discussed in Komori and Shimada (1995).

Toba and Kunishi (1970) estimated the drag coefficient γ_{10}^2 at the air-water interface from the water-surface wind stress measured in three wind-wave tunnels with various fetches and plotted the drag coefficient against the Reynolds number on the air side, $Re = u^*H/\nu$, based

on the friction velocity on the air side and the wave height, H. The drag coefficient gradually increased up to Re = 100 and it almost leveled off in the range of 100 < Re < 1,000. When the Reynolds number was over 1,000, the coefficient rapidly increased with increasing Re. This behavior was quite similar to the variation of the CO_2 transfer velocity with Reynolds number (Komori et al. 1995a; Komori and Shimada 1995). The similarity between the results of these independent approaches supports the reliability of the k_L - wind speed relationship described here.

2.4 Relationship Between Turbulence Structure and the CO_2 Transfer Mechanism

2.4.1 Turbulence structure near a sheared wavy air-water interface

To physically explain the behavior of k_L (Fig.8), the turbulence structure near a sheared wavy air-water interface was investigated by means of both a flow visualization technique (Komori et al. 1993a) and a direct numerical simulation (Komori et al. 1993c; Nagaosa and Komori 1995). The organized motions above and below the air-water interface were visualized with paraffin smoke and a laser dye in high-speed video pictures (Fig.9). Organized motion in the air flow above the interface intermittently appears in front of wave crests and generates the upward accelerated bulge of smoke which was also shown by Kawamura and Toba (1988). The organized motion in the air flow above the highly sheared wavy interface is generated by a two-dimensional wave. The generation mechanism is different from bursting phenomena observed near smooth rigid walls, since the intermittent organized motion is always observed in front of wave crests (Fig.9). In contrast, Rashidi and Banerjee (1990) and Banerjee (1990) observed streaky structures at the non-wavy gas-liquid interface in a counter-current air-water open-channel flow with high interfacial shear, which were quite similar to those found near rigid walls. They suggested that the bursting motions are generated in the interfacial region of the water flow. Furthermore, they estimated a bursting frequency which is proportional to u^{*2}. This bursting structure may be right for weakly sheared interfaces with waves of small height close to the non-wavy interface. However, for a highly sheared interface with comparatively large wave heights, the turbulence structure rather resembles the structure above a solid wavy wall (dashed lines in Fig.9), though neither air separation nor recirculating flow behind the wave crest could be clearly visualized because of the difficulty of introducing smoke into wave valleys.

In the water, the surface-renewal motion appears intermittently and frequently and it renews the free surface like a rolling eddy. The frequency of appearance of surface-renewal eddies in high shear region is far larger than the typical frequency of the waves. The scale of such surface-renewal eddies is roughly estimated to be 0.05~0.5λ, where λ is the wave length. The surface-renewal motion is generated below the interface at the same place where the organized motion in the air flow occurs (Fig.9). This observation suggests that surface renewal motion in the water flow is induced in the front of wave crests by strong shear due

to organized motion in the air flow. In addition to the surface-renewal motion, strong downward bursts with a large-scale which spirally intrude into the bulk water are intermittently observed (Fig.9). Such bursts are likely to be associated with wave motion, and their values of frequency of appearance and scale are roughly equivalent to those of wave frequency and wave length. Similar large-scale downward bursts were also observed by Yoshikawa et al. (1988). Such bursts may be produced by the drift of three-dimensional waves through a kind of the Langmuir circulation drive mechanism.

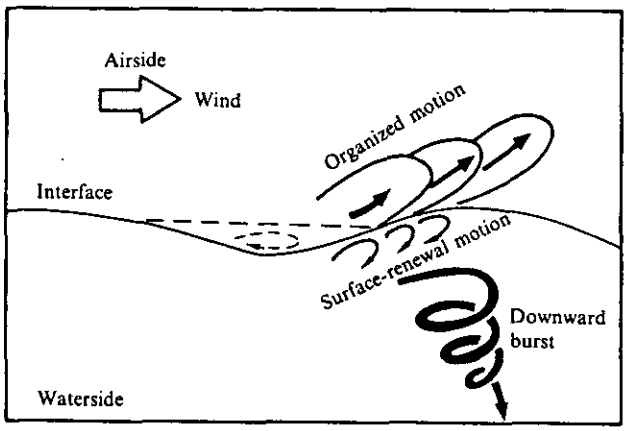

Figure 9. Sketch of the organized motions above and below the wave (Komori et al. 1993a).

The turbulence structure described above (Fig.9) can be confirmed by DNS. The instantaneous air and water velocity vectors for a sheared wavy air-water interface (Figs. 10 and 11) clearly show the upward organized motion over the interface and the surface renewal eddy beneath the interface. The locations where the upward and surface renewal organized motions are generated in the air and water flows correspond well to the region with the maximum shear stress and pressure as shown in the predictions of instantaneous shear stress and pressure at the interface (Fig. 12). The DNS predictions support the inference from the experimental results that surface renewal eddies are generated by strong shear acting on the front of the wave crests.

Both the organized upward motion in the air flow and the spiral downward burst in the water flow (Fig.9) can also be explained by the DNS for the air flows over two and three dimensional rigid wavy walls. The distributions of the instantaneous shear stress and pressure on two dimensional wave wall (Fig.13) are quite similar to those at a sheared wavy air-water interface (Fig.12). The instantaneous velocity vectors over the two dimensional wavy wall also show the presence of upward organized motion similar to that observed in an air flow over an air-water interface (Fig.14). When a tracer is periodically introduced into the air flow over wavy wall, we can see that the organized motion has a spiral structure (Fig.15).

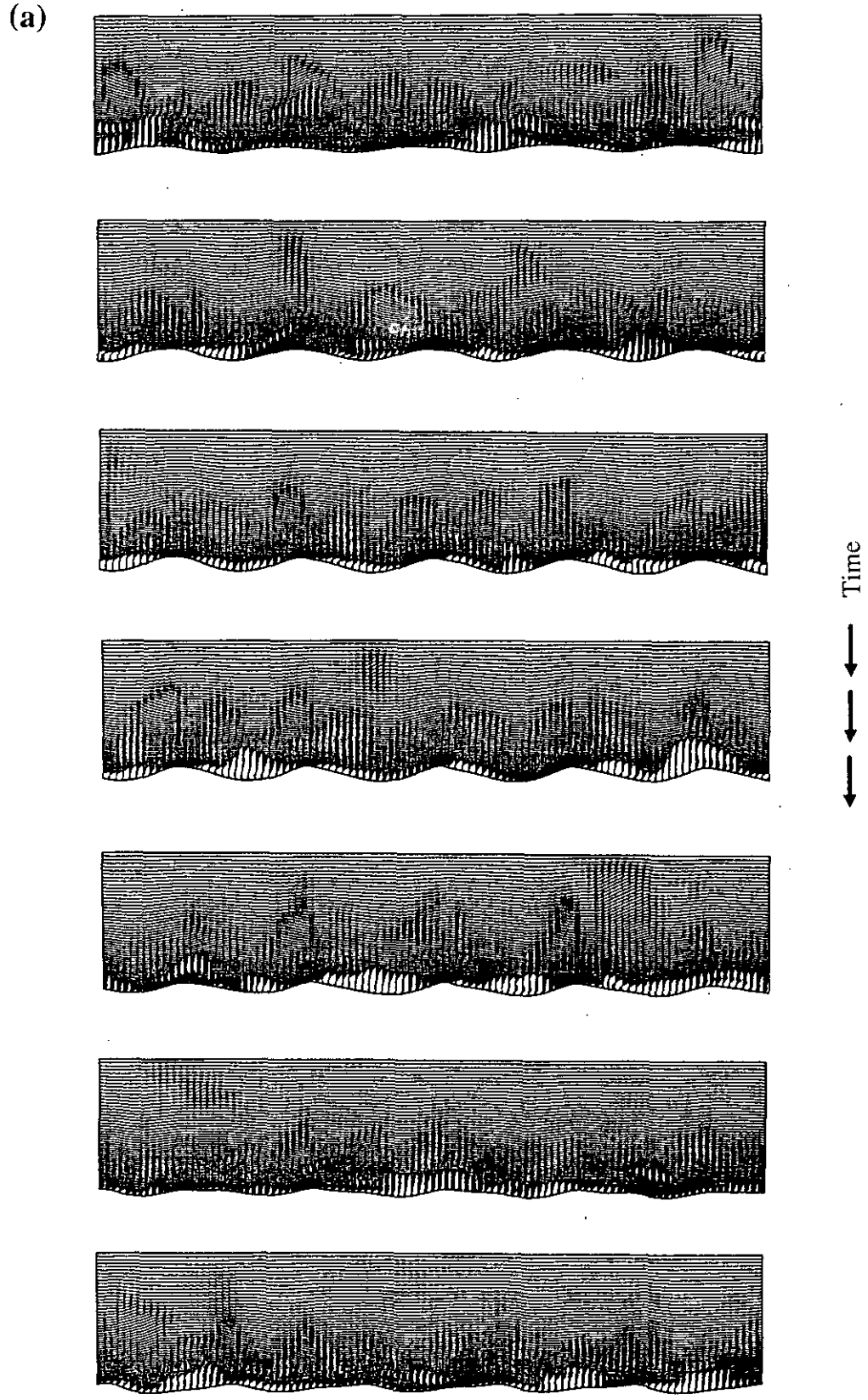

Figure 10. Time variations of instantaneous air and water velocity vectors for a sheared wavy air-water interface: (a) velocity vectors in the air flow.
(Nagaosa and Komori 1995)

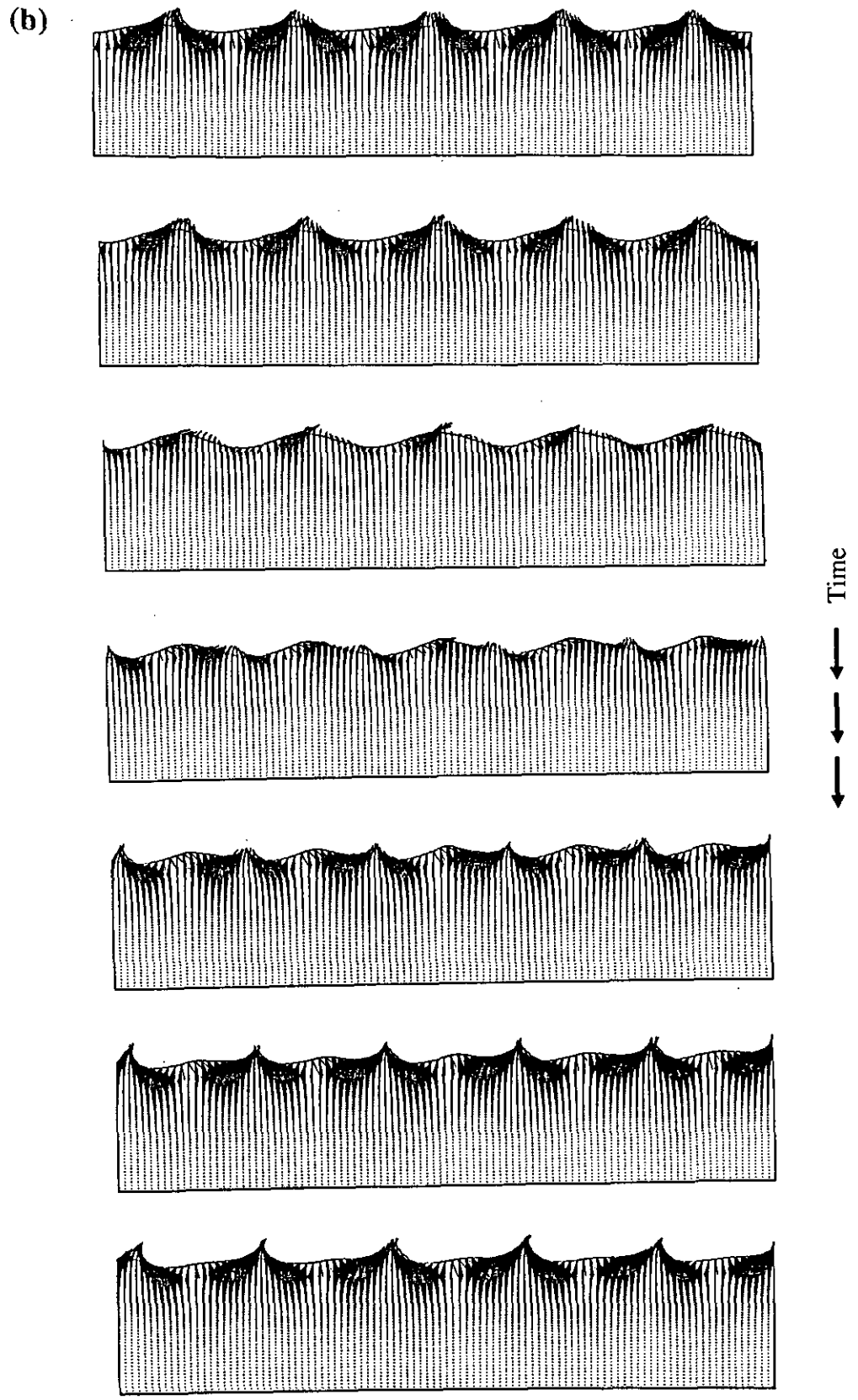

Figure 10. Time variations of instantaneous air and water velocity vectors for a sheared wavy air-water interface: (b) velocity vectors in the water flow. (Nagaosa and Komori 1995)

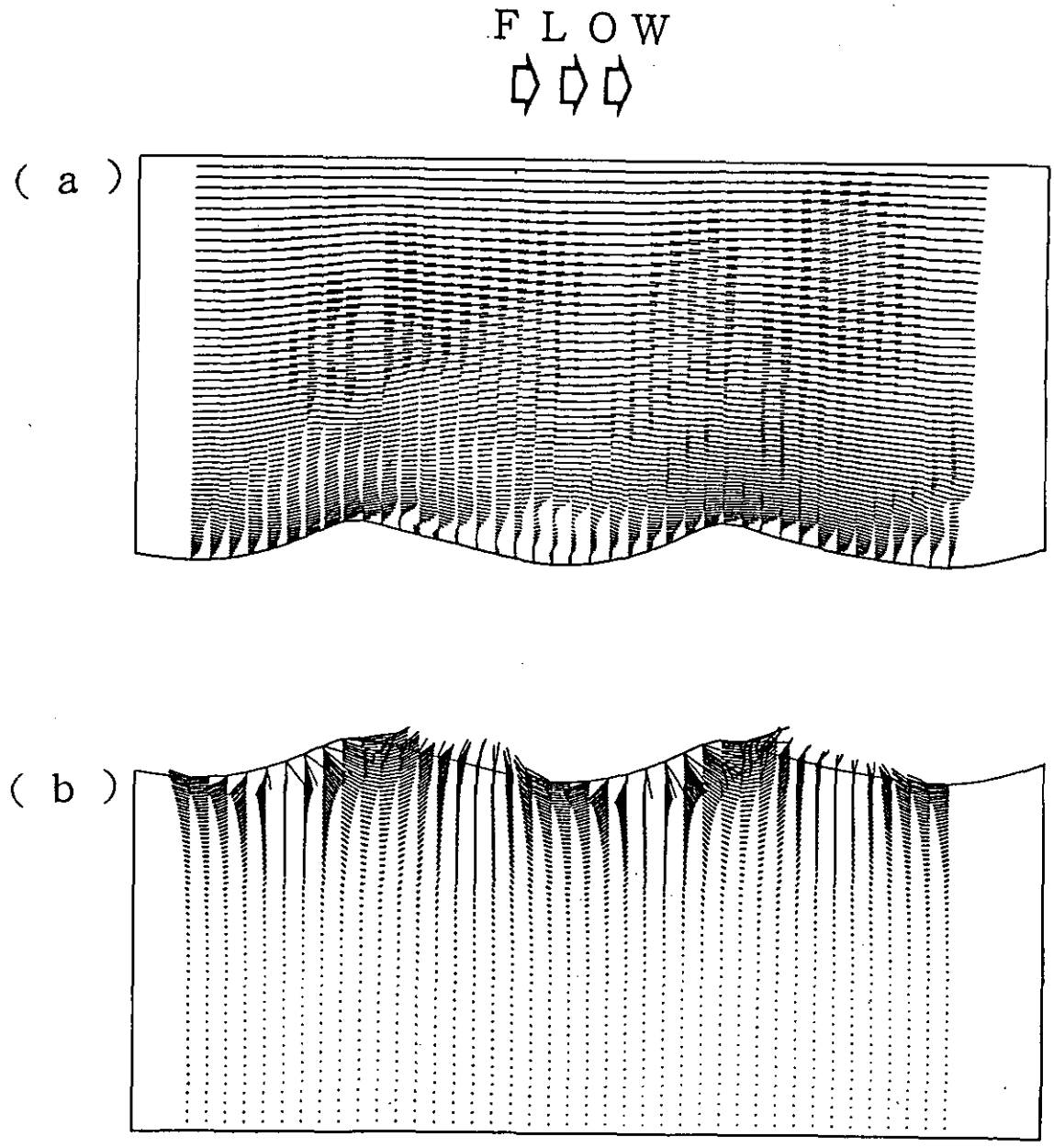

Figure 11. Instantaneous air and water velocity vectors near a sheared wavy air-water interface: (a) air velocity vectors showing an upward organized motion in the air flow; (b) water velocity vectors showing a surface renewal eddy in the water flow. (Nagaosa and Komori 1995)

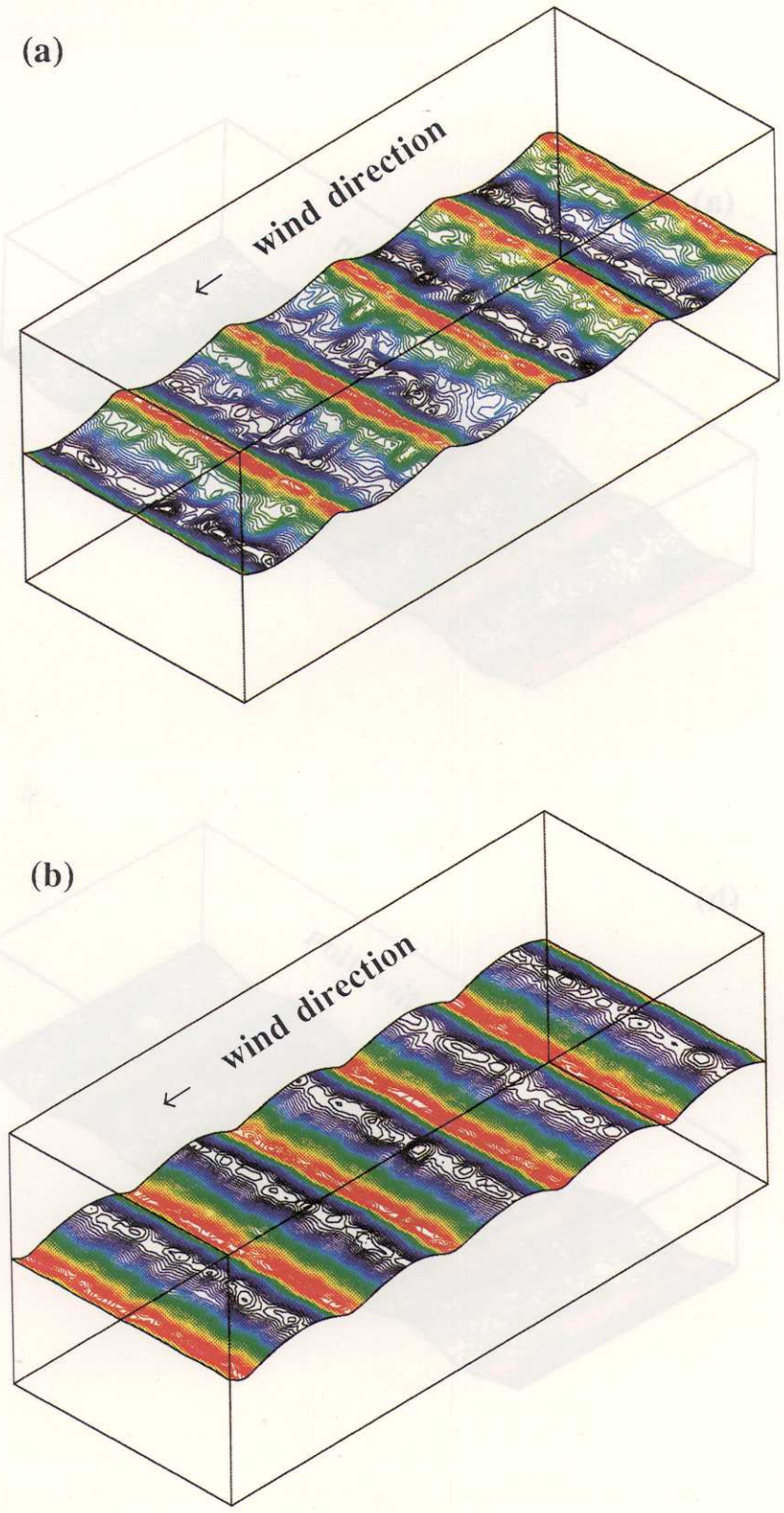

Figure 12. Instantaneous shear stress and pressure at a sheared wavy air-water interface: (a) shear stress; (b) pressure. (Nagaosa and Komori 1995)

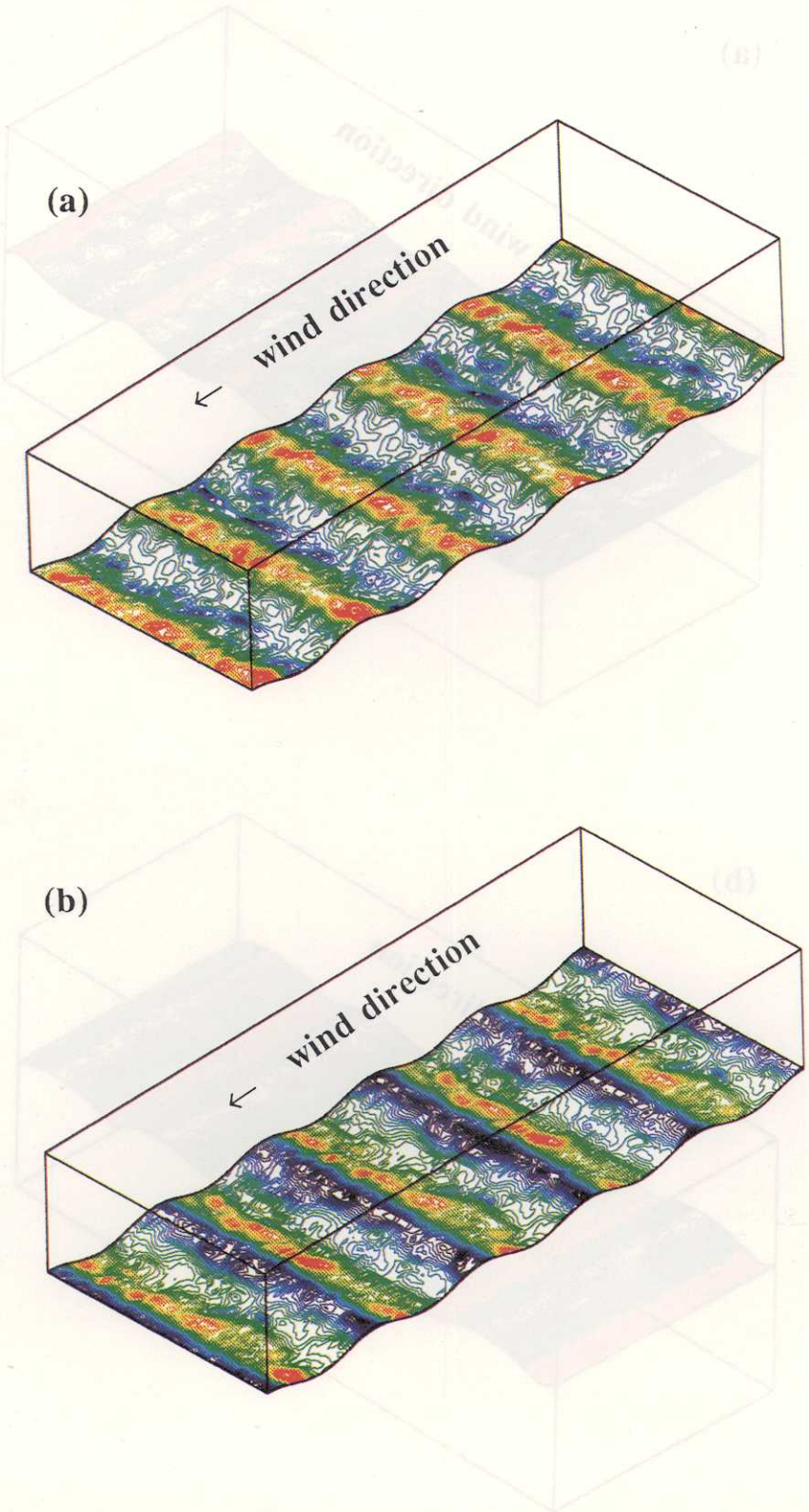

Figure 13. Instantaneous shear stress and pressure on a two dimensional wavy wall:
(a) instantaneous shear stress; (b) instantaneous pressure.
(Komori et al. 1993c)

The distributions of the instantaneous shear stress and pressure on a three dimensional wavy wall (Fig.16) are quite different from those on a two dimensional wavy wall. Unlike the case for the two dimensional wavy wall (Fig.15), organized upward motion over a three dimensional wavy wall could not be discerned with periodic tracer introductions (Fig.17). The flow was accelerated around the root of each wave, generating high shear stress and pressure there. However, the magnitude of the instantaneous shear stress acting on a three dimensional wavy wall differs between the left and right hand sides (Fig.18). This difference is caused by the imbalance of the shear stresses between left and right hand sides, and in the case of an air-water interface, a spiral motion may be generated in the water flow beneath the free surface. This suggests that spiral downward bursts (Fig.9) occur when two dimensional waves are intermittently changed into three dimensional waves. Thus, the DNS for rigid wavy walls and an air-water interface can explain the experimental results well.

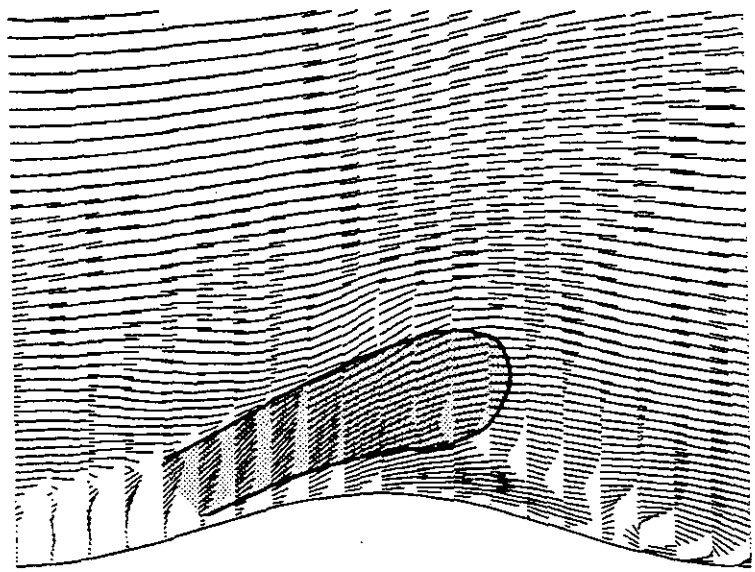

Figure 14. Upward organized motion in the air flow over a two dimensional wavy wall. (Komori et al. 1993c)

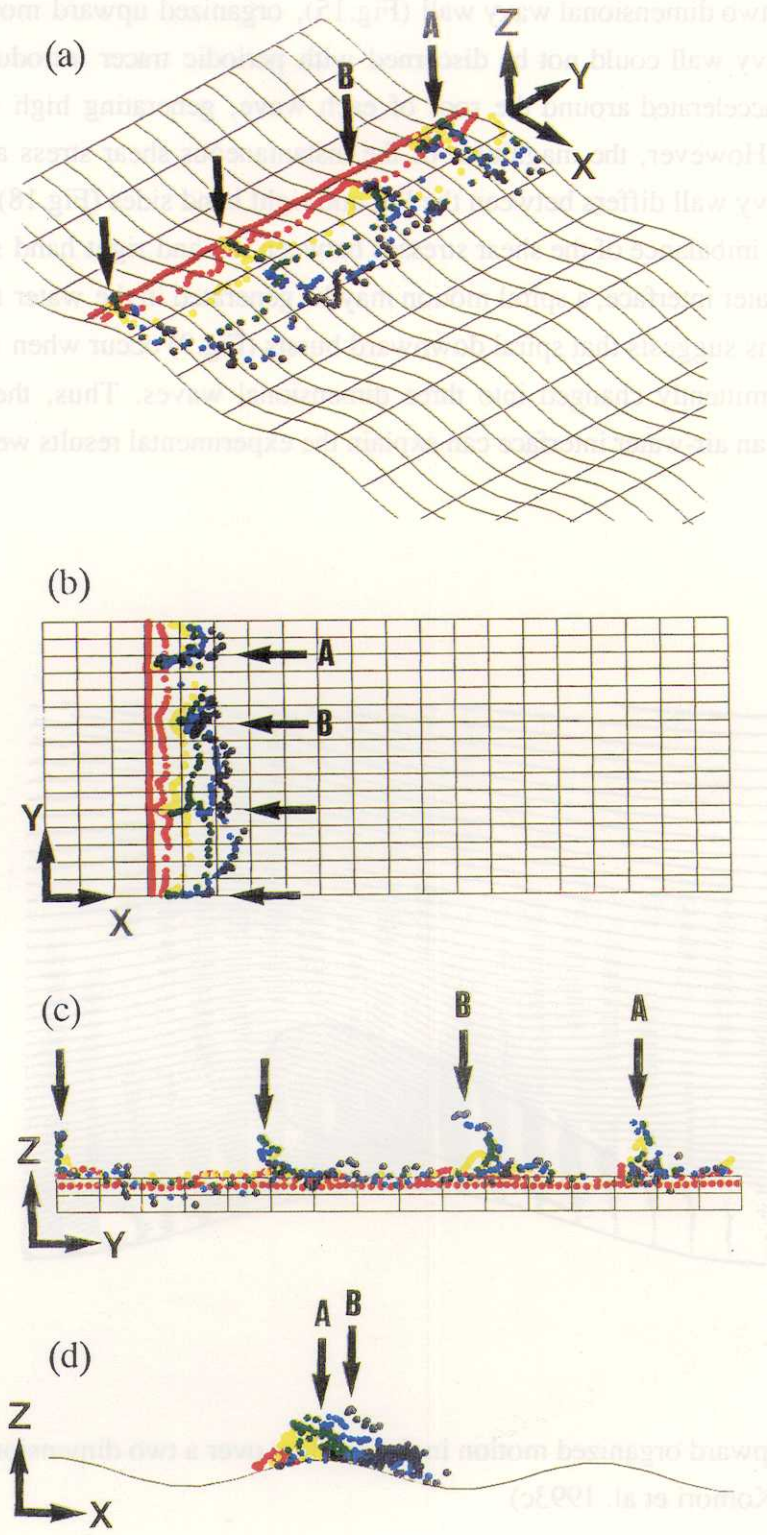

Figure 15. Movements of a passive tracer periodically introduced into the flow over a two dimensional wavy wall: (a) three dimensional view; (b) upward view; (c) spanwise view; (d) side view. (Nagaosa 1995; Komori et al. 1993c)

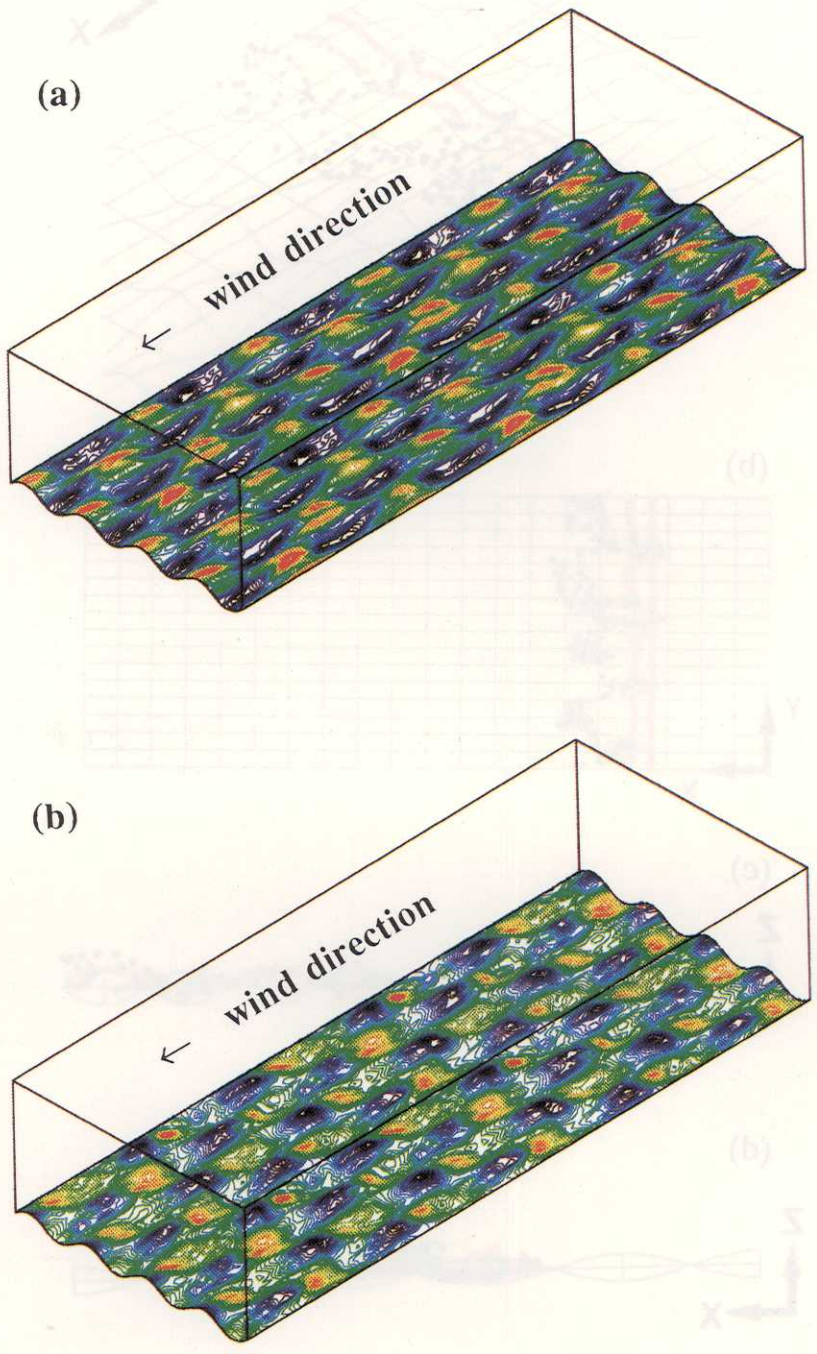

Figure 16. Instantaneous shear stress and pressure on a three dimensional wavy wall:
(a) instantaneous shear stress; (b) instantaneous pressure.
(Nagaosa 1995)

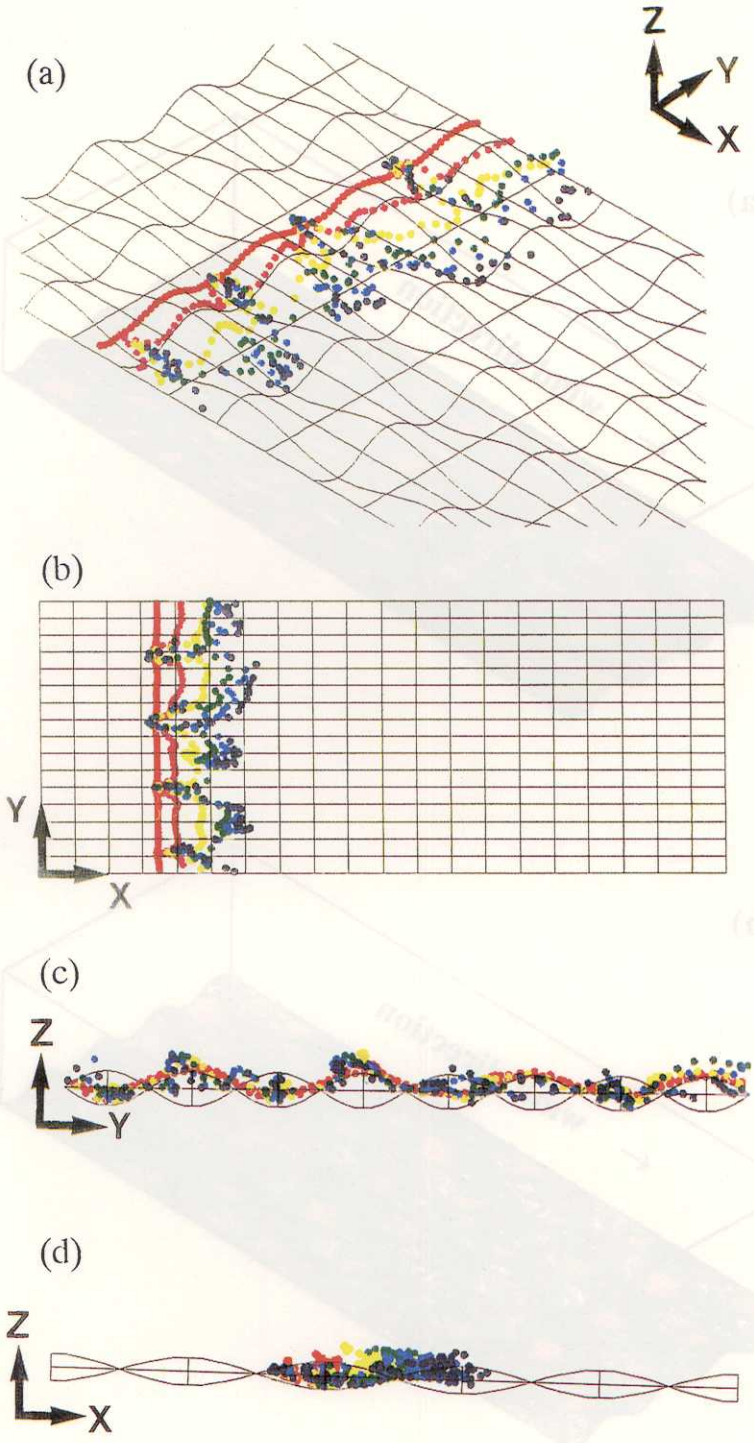

Figure 17. Movements of a passive tracer periodically introduced into the flow over a three dimensional wavy wall: (a) three dimensional view; (b) upward view; (c) spanwise view; (d) side view. (Nagaosa 1995)

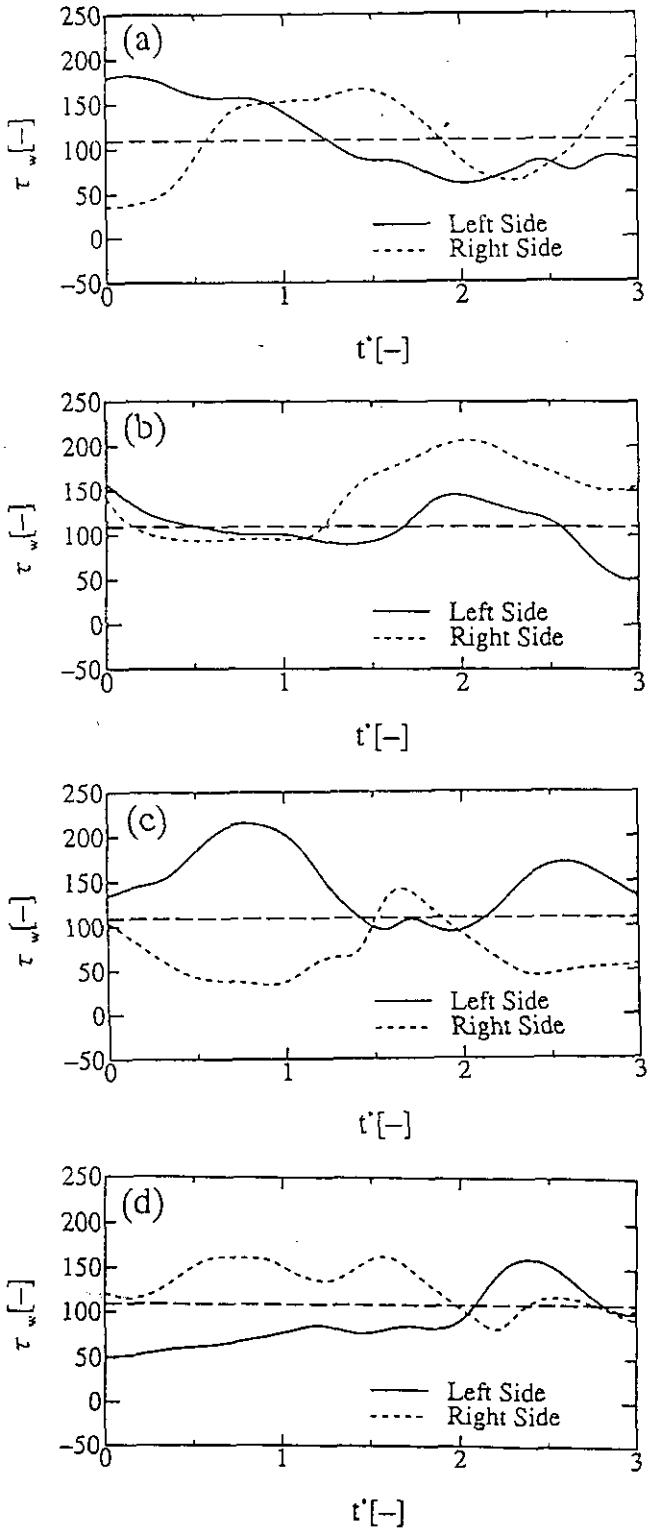

Figure 18. Instantaneous shear stress distributions on the right and left hand sides around a three dimensional wavy wall at several times (a)~(d). (Nagaosa 1995)

2.4.2 Mechanism of CO_2 transfer across a sheared, wavy air-water interface

Figure 19 shows the predictions of instantaneous concentration of CO_2 at a sheared, wavy air-water interface while being absorbed from air flow to water flow. The CO_2 concentrations rise just behind the wave crests where the surface renewal eddies are brought down into the water flow. This result means that the organized surface renewal motion in the water flow controls largely mass transfer across the air-water interface.

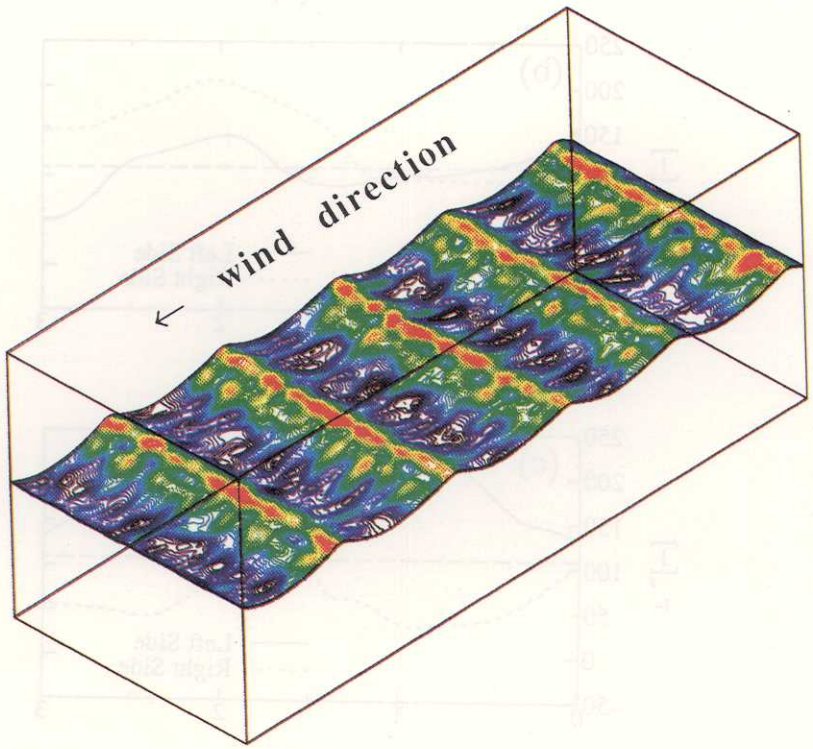

Figure 19. Predictions of instantaneous CO_2 concentration at a sheared wavy air-water interface. (Nagaosa and Komori 1995)

To estimate the frequency of appearance of the organized motions discussed above, a well-known VITA (Variable Interval Time-Averaging) technique was applied to the streamwise velocity signals in the air and water flows (Komori et al. 1993a). The frequencies of appearance of the organized motions in the air and water flows, f_G and f_L, were plotted against the wind friction velocity on the air side (Fig.20) (Komori et al. 1993a). Both frequencies increase with increasing u^*, and for shear $u^* > 0.25$ m/s, f_G is in good agreement with f_L. However, for shear $u^* < 0.25$ m/s, the frequencies deviate from each other, and f_G becomes larger than f_L. In other words, the organized motions appear more

frequently in the air flow than in the water flow. This result suggests that only strong organized motions with high turbulent shear in the air flow can induce organized motions in the water flow. When considering the turbulence generation mechanism in a wind-wave tank (see Fig.9), we can easily accept this assumption. The uv-quadrant method (see Alfredsson and Johansson 1984) was used to educe strong organized motions with large momentum in the air flow (Komori et al. 1993a).

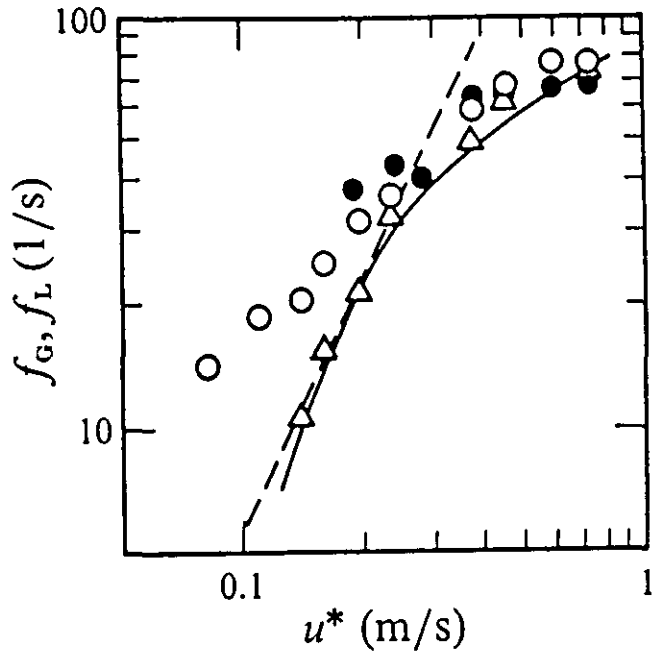

Figure 20. Variations of the frequencies of appearance of organized motions with friction velocity (Komori et al. 1993a) :
O, f_G in the air flow; Δ, f_L in the water flow; ● , f_G estimated by flow visualization in the air flow. The solid line shows the frequency of appearance of the strong organized motions in the air flow, f_{GS}, detected by the uv-quadrant method. The dashed line shows proportionality between f_L and u^{*2}.

The frequency of appearance of strong organized motions, f_{GS}, (solid line in Fig.20) is in good agreement with the frequency of the organized motion on the water side over the whole range of u^* values. This agreement supports the assumption that only strong organized motions with large Reynolds stress in the air flow can induce organized motions in the water flow. To show that the organized motions in the air flow visualized as in Fig.9, correspond to the organized motions detected by the above described VITA technique, the occurrences of

the smoke bulges observed in the air flow were counted by eye as objectively as possible by freezing each frame of the high-speed video pictures. The frequency of the organized motion counted from the flow visualization in the air flow (shown by solid circles in Fig.20) agrees well with the frequency detected by the VITA technique.

It should be noted that f_L and f_{GS} increase in proportion to the square of u^* in the weakly sheared region of $u^* < 0.25$ m/s (dashed line in Fig.20), and the rate of increase with u^* decreases at high shear with $u^* > 0.25$ m/s. The proportionality for weak shear is in good agreement with the results of Rashidi and Banerjee (1990) and Rashidi et al. (1991) for an open-channel flow with a non-wavy sheared interface. This concurrence of results suggests that for weak shear with small waves, the main mechanism of turbulence production is similar to the bursting phenomena found by Rashidi and Banerjee (1990), but that for high shear with bigger waves, the turbulence is generated by the waves themselves (Fig.9). Therefore, the frequencies of the organized motions cannot be estimated as a simple function of u^*.

Komori et al. (1989; 1990) and Komori (1991) showed that the organized motions appearing in the interfacial region on the liquid side renew the interface and control the mass transfer in open-channel flows with zero-shear interfaces. Their experiments on the absorption for CO_2 and Ar gases also showed that the relation between the mass transfer velocity k_L and surface-renewal frequency f_S ($=f_L$) on the liquid side is approximated by

$$k_L = 0.34\sqrt{D_L f_S}\,, \tag{27}$$

where D_L is the molecular diffusivity of gas on the liquid side. The value of 0.34 is an empirical constant and it may depend on the condition of the air-water interface (Komori and Shimada 1995; Shimada and Komori 1996). When the organized motion induced on the water side renews the sheared interface in a wind-wave tank, it also controls the mass transfer. Therefore, the measurements of k_L in a wind-wave tank were well correlated by Eq.(27). To explain the behavior of k_L in Fig.8, the values of $f_S^{1/2}$ calculated by Eq.(27) together with the measurements of k_L are compared with the measurements of $f_S^{1/2}$ in Fig.21 (Komori et al. 1995a). The measured values of $f_S^{1/2}$ agree well with the estimated values at wind speeds less than 12 m/s. However, at wind speeds greater than 12 m/s, the measured values of $f_S^{1/2}$ become smaller than the estimated values. The difference may be caused by the intense enhancement of CO_2 transfer by a great number of ripple-like surface renewal eddies generated by intense wave breaking. However, the scales of the ripple-like eddies were smaller than half of the wave heights and it was difficult to detect the ripple-like motions by means of the same velocity measurement techniques. Thus, it was concluded that organized surface renewal eddies (Fig.9) control the CO_2 transfer across a sheared air-water interface.

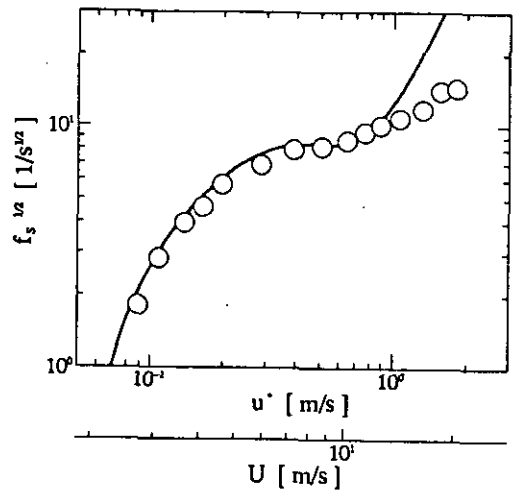

Figure 21. The square root of frequency of appearance of the surface renewal eddies as a function of U or u^* (Komori et al. 1995a; Komori and Shimada 1995). The circles show the measurements and the solid line indicates the values estimated from both Eq.(27) and the measured k_L in Fig.8.

2.4.3 Estimation of CO_2 transfer velocity across the air-sea interface

Komori et al. (1995a) and Komori and Shimada (1995) measured the CO_2 transfer velocity for five water types - pure, filtered tap, natural sea, artificial sea and 3.5 wt% salt waters in an oscillating-grid tank. Plotting the measurements against the frequency of appearance of surface renewal eddies (Fig.22) (Komori et al. 1995a; Komori and Shimada 1995) shows that the CO_2 transfer velocity for sea and salt waters is damped to about 50% of that for fresh waters. The reason why the transfer velocity for sea and salt waters is drastically reduced is discussed in Komori and Shimada (1995). By taking this damping factor of 0.5, the CO_2 transfer velocity across the air-sea interface, k_{LS}, was given by

$$k_{LS} \approx 0.5 k_L \ , \tag{28}$$

where k_L is the transfer velocity for fresh water (Fig.22). However, the dependency of the damping factor on the wind speed could not be investigated in an oscillating-grid tank and the problem remains as a future work. In fact, our recent measurements for 3.5wt% salt water in a wind-wave tank showed that the value of the damping factor in Eq.(28) rapidly increases at wind speeds larger than 4m/s, since the effect of surface-active impurities is weaken by wave-breaking phenomena (Shimada and Komori 1996). The estimated values of the CO_2 transfer velocity based on a constant damping factor of 0.5 in Eq. (28) (Fig.23: solid circles) are included by the higher values of previous field measurements at wind speeds less than 5 m/s and they are rather larger than those estimated by the proportional relationship between U and k_L proposed by Liss and Merlivat (1986) (Fig.23: dashed line). If a more accurate

damping factor larger than 0.5 is used for wind speeds larger than 4m/s, the difference between our estimation and the relationship of Liss and Merlivat (1986) will become larger even in the wind speed range of U > 5 m/s. The relationship of Liss and Merlivat (1986) has been used in most general circulation models (GCMs). However, our results (Fig.23) suggest that the previous simulations based on these GCMs rather underestimate the rate of CO_2 exchange between the atmosphere and the ocean.

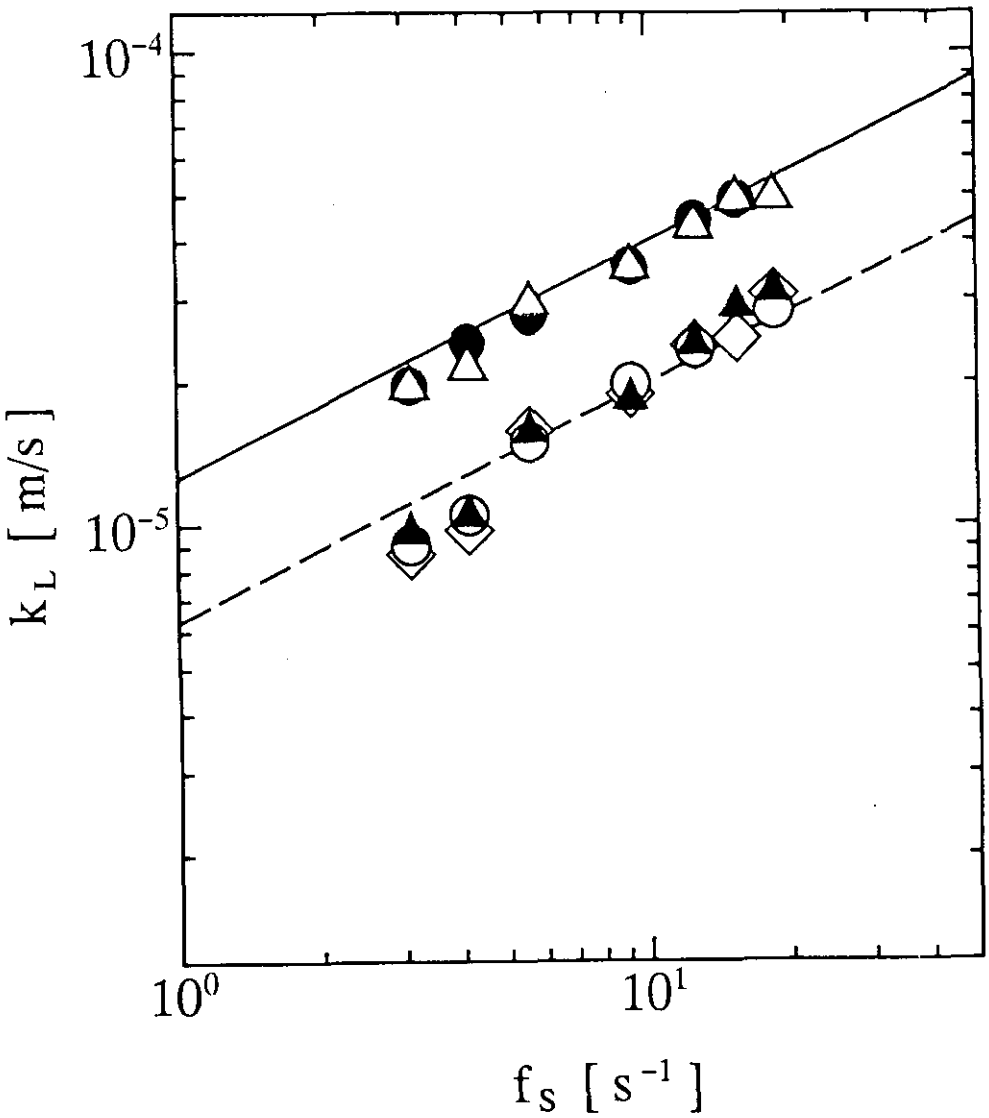

Figure 22. Variations of the CO_2 transfer velocity for five waters against the frequency of appearance of surface renewal eddies (Komori et al. 1995a; Komori and Shimada 1995).
●, tap water; Δ, pure water; O, 3.5 wt% saltwater; ▲, natural sea water; ◇, artificial sea water.
The solid line shows Eq.(27) and the dashed line indicates the values of the solid line multiplied by 0.5.

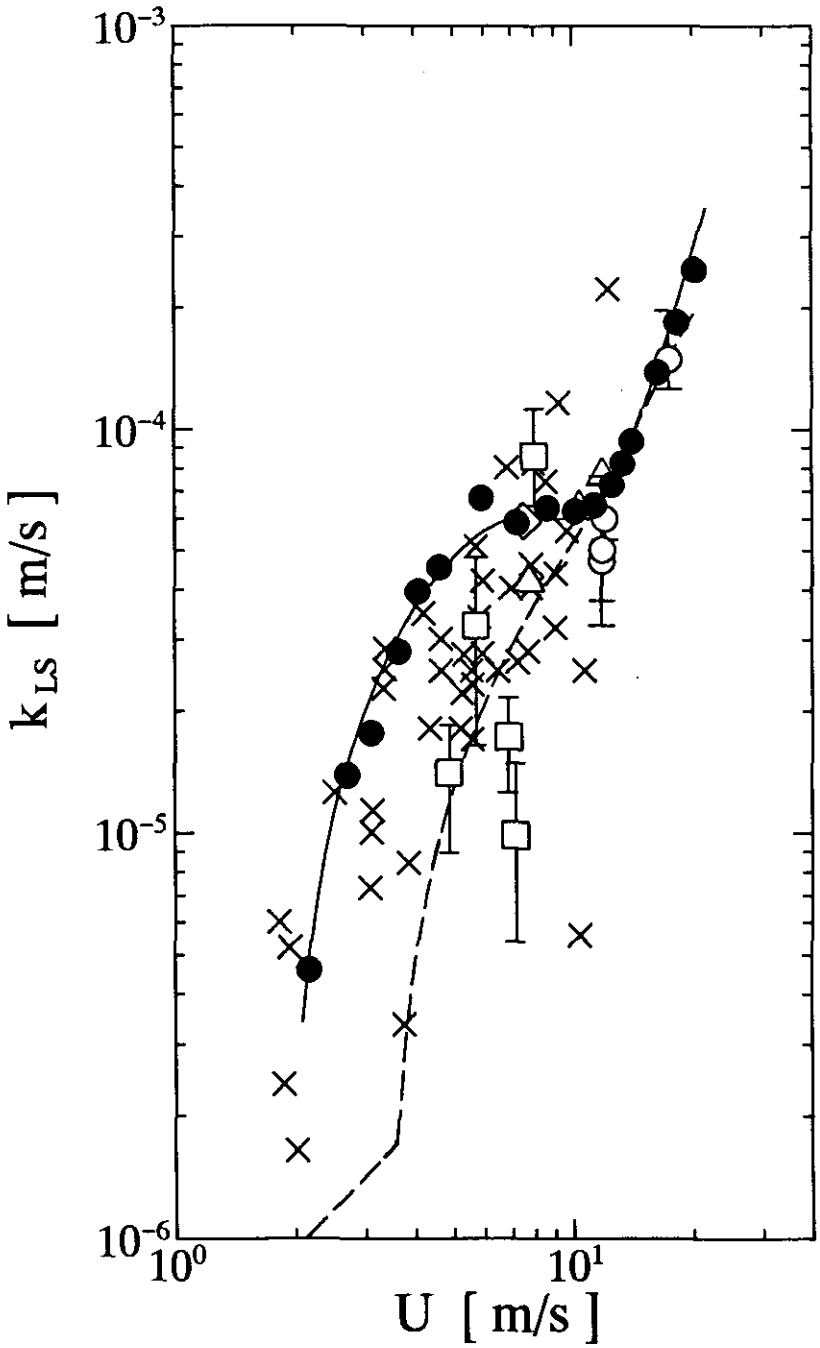

Figure 23. Comparison of the relationship between air-sea CO_2 transfer velocity and wind speed; (●) estimated in this project and (other symbols) previous field measurements (other symbols) (Komori and Shimada 1995).
The solid line shows a best-fit curve for the estimated values and the dashed line indicates the proportional relationship between U and k_L published by Liss and Merlivat (1986).